Vibrational excitation and dissociation processes in high-temperature N_2-O_2 state-to-state collisions based on neural network and dynamic simulation*

GUO Changmin[1], ZHANG Hong[2], CHENG Xinlu[1†]

1.Institute of Atomic and Molecular Physics, Sichuan University, Chengdu 610065, China

2.College of Physics, Sichuan University, Chengdu 610065, China

Abstract

The scattering cross-sections and reaction rate coefficients are crucial parameters for elucidating the energy transfer mechanism of state-to-state collisions between molecular gases and also serve as a fundamental basis for modeling the non-equilibrium flow field. However, the database of kinetic processes related to nitrogen shock flows is still being developed. In this work, a detailed kinetic study of the N_2+O_2 collision is carried out by combining the quasi-classical trajectory method (QCT) and neural network model (NN). Firstly, QCT is used to calculate 90 initial vibrational state combinations (v, w) for N_2+O_2 collisions, and the contributions of all vibrational excitation and dissociation reaction channels are discussed. The following conclusions are drawn: 1) The contributions of the vibration-vibration (VV) energy exchange channel of O_2 and N_2 are similar, while the vibration-translational (VT) transition mainly occurs on O_2; 2) The total dissociation cross-section primarily results from the O_2 single-dissociation channel, followed by the exchange-dissociation channel, with relatively minor contributions from the N_2 single- and double-dissociation channels. Then, based on the QCT dataset, a high-performance NN model (R-value of 0.99) is trained to predict the total dissociation cross-section caused by $N_2(v)$+$O_2(w)$ collisions. Compared with the method that only uses QCT, the method that jointly uses QCT and NN model can achieve an approximately 91.94 % reduction in computational cost. Finally, to facilitate use in kinetic modeling, Arrhenius-type fits for the VV/VT rate coefficients are provided over the temperature range of 5000–30000 K, and an exponential form related to the translational energy E_t is used to fit the total dissociation cross-section.

Keywords: state-to-state reaction rate coefficient, vibration relaxation, collision dissociation, neural network model.

PACS: 34.50.–s, 34.50.Ez, 34.80.Ht

doi: 10.7498/aps.74.20250533

cstr: 32037.14.aps.74.20250533

---

* The paper is an English translated version of the original Chinese paper published in Acta Physica Sinica. Please cite the paper as: **GUO Changmin, ZHANG Hong, CHENG Xinlu, Vibrational excitation and dissociation processes in high-temperature N_2-O_2 state-to-state collisions based on neural network and dynamic simulation.** *Acta Phys. Sin.,* 2025, 74(15): 153401. doi: 10.7498/aps.74.20250533

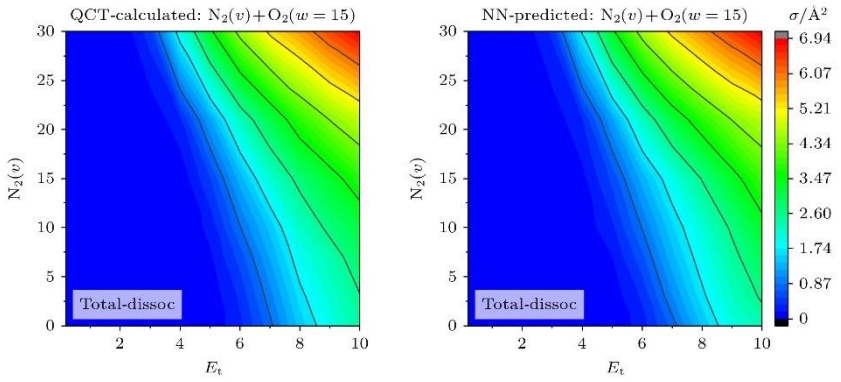

1. Introduction

The flow field around a hypersonic vehicle can reach temperatures exceeding 20000 K, where components undergo a series of complex dynamic and chemical processes such as vibrational excitation, dissociation, and ionization. These processes significantly impact the vehicle's mechanical and thermal performance[1–4]. In such high‐temperature environments, the coupling of numerous relaxation processes and chemical reactions drives the fluid into a state of strong thermochemical non‐equilibrium, posing major challenges for dynamic modeling. Among these processes, the vibrational degree of freedom profoundly affects molecular interactions and physical properties, playing a key role in inelastic collision energy transfer, dissociation, and exchange reactions[5–7]. Therefore, investigating state‐to‐state (STS) collision energy transfer in high‐temperature non‐equilibrium flows is essential. The results are crucial for diagnosing such flow fields and advancing aerospace technology.

Kinetic simulation plays a vital role in high‐temperature gas dynamics due to the difficulty and high cost of ground experiments. The STS method operates at the atomic and molecular level to study collision and reaction rules between different energy states of each gas component, overcoming the empirical limitations of traditional models. It has been widely used in plasma, atmospheric, combustion, and non‐equilibrium gas simulations[8,9]. In the STS model, the equations for solving the energy‐level populations of each component require the rate coefficients of all vibrational‐rotational transitions and dissociation/exchange processes; thus, the model's accuracy strongly depends on the accuracy and completeness of these rate coefficients. In recent years, researchers worldwide have sought to reveal the vibrational energy‐transfer mechanisms in high‐temperature non‐equilibrium gas collisions with higher precision through advanced spectroscopy and quantum‐mechanical simulations[10–13], especially the STS collision processes of the nitrogen‐oxygen system, which are the main components of Earth's atmosphere[14–17]. Compared with collisions between identical molecules (e.g., N_2-N_2, O_2-O_2), the fundamental collision processes of N_2-O_2 are far more complex, involving the following six main vibrational‐excitation and dissociation channels ($\Delta v > 0$):

1) Inelastic vibration-translation (VT) transitions, comprising vibrational de‐excitation of N_2 (VTN) and of O_2 (VTO):

$$\text{VTN}: N_2(v)+O_2(w) \rightarrow N_2(v\text{-}\Delta v)+O_2(w) \quad (1)$$

$$\text{VTO}: N_2(v)+O_2(w) \rightarrow N_2(v)+O_2(w\text{-}\Delta v) \quad (2)$$

2) Inelastic vibration-vibration (VV) transitions, comprising energy transfer from N_2 to O_2 (VVN) and from O_2 to N_2 (VVO):

$$\text{VVN}: N_2(v) + O_2(w) \rightarrow N_2(v\text{-}\Delta v)+O_2(w+\Delta v) \quad (3)$$

$$\text{VVO}: N_2(v) + O_2(w) \rightarrow N_2(v+\Delta v)+O_2(w\text{-}\Delta v) \quad (4)$$

3) Single O_2 dissociation reaction:

$$N_2(v)+O_2(w) \rightarrow N_2(v')+2O \quad (5)$$

4) Single N_2 dissociation reaction:

$$N_2(v)+O_2(w) \rightarrow 2N+O_2(w') \quad (6)$$

5) Exchange-dissociation reaction producing one NO molecule:

$$N_2(v)+O_2(w) \rightarrow NO(v')+N+O \quad (7)$$

6) Double dissociation reaction:

$$N_2(v)+O_2(w) \rightarrow 2N+2O \quad (8)$$

Here v and w are the initial vibrational quantum numbers of N_2 and O_2, respectively, and the primed symbols (e.g., v', w') denote the vibrational levels of product molecules after collision. In the inelastic collision VV/VT processes (1)-(4), Δv represents the change in vibrational quantum number of the molecule; $\Delta v = 1$ is termed a single- quantum transition, while $\Delta v = 2,3$ are multi- quantum transitions. Based on the ab initio potential energy surface of the electronic ground state of the N_2O_2 system[18], the N_2 molecule occupies approximately 9181 vibration- rotation states ($v_{max} = 54$), while the O_2 molecule occupies about 2950 such states ($w_{max} = 36$). Consequently, roughly 3×10^8 distinct STS processes need to be considered for $N_2(v, j)$ -$O_2(w, n)$ collisions, which is infeasible to calculate exhaustively. Most previous studies have been restricted to collisions between two identical excited states ($v = w$) or combinations involving a ground state ($v = 0$ or $w = 0$)[19–22]; investigations of the energy-transfer mechanisms for vibrational excitation and dissociation in general collisions ($v \neq w \neq 0$) remain relatively scarce. Taking VV transition as an example, earlier quantum[23] and semiclassical[24] calculations focused mainly on the single- quantum processes $(1, 0 \mid 0, 1)$ and $(0, v \mid 1, v–1)$. More recent studies have either discussed only the same transition processes or provided results limited to the higher temperature range of 8000–20000 K[21,25,20].

With the rapid advancement of artificial intelligence, machine- learning techniques have been introduced into the study of collision energy transfer in high- temperature gases. Based on limited datasets obtained by the quasi- classical trajectory (QCT) method, neural- network (NN) models are trained to fill gaps in unexplored regions of parameter space, greatly improving the computational

efficiency of traditional dynamics while preserving accuracy. For instance, Koner *et al.*[26] used an NN model to predict STS exchange-reaction cross sections for $N(^4S)+NO(^2\Pi) \rightarrow N_2(X^1\Sigma^+_g)+O(^3P)$, achieving a correlation coefficient R of 0.99; Chen *et al.*[27] employed Gaussian-process regression to effectively predict vibrational inelastic VV transition cross sections for CO(v)+CO(v) collisions. Hong *et al.*[28] used an NN model to obtain a complete VT rate-coefficient dataset for $N_2(v)+H_2(0) \rightarrow N_2(v-\Delta v)+H_2(0)$ ($\Delta v = 1,2,3$); Gu *et al.*[29], Huang *et al.*[30], and Guo *et al.*[31] applied trained NN models to predict designated-state dissociation cross sections for N_2+N and O_2+N systems[29,30] and inelastic VV/VT reaction cross sections for the $N_2(v_1)+N_2(v_2)$ system[31], respectively, all achieving $R \approx 0.99$. Compared with atom-molecule collision systems, the application of NN models to molecule-molecule collisions is more challenging. This is because the energy-transfer mechanisms of inelastic VV/VT transitions and dissociation/exchange reactions, as well as their coupling effects, may differ in STS collisions involving distinct initial vibrational levels. Therefore, building NN predictive models for different reaction channels may require distinct kinetic input features and training datasets, necessitating a systematic investigation of the contributions from individual reaction channels and the evolution of kinetic parameters across different energy degrees of freedom.

In this work, we systematically study the inelastic VV and VT transitions as well as various dissociation processes in N_2-O_2 collisions by combining QCT calculations with an NN model. The paper is structured as follows: Section 2 describes the QCT computational details and the neural-network model; Section 3 discusses the inelastic VV/VT reaction cross sections and rate coefficients, the cross sections of each dissociation channel, and the NN model for predicting total dissociation cross sections of designated-state collisions; and Section 4 presents the conclusions.

2. Theoretical calculation method

2.1 Quasiclassical trajectory method

The quasi-classical trajectory method[32,33] applies quantum mechanics to describe the initial and final vibration-rotation states of molecules within the Born–Oppenheimer approximation, while treating molecular collision trajectories classically. It solves Hamilton's equations of motion to obtain the trajectory of each nucleus on the potential energy surface; dynamical information of the reaction system is then obtained from statistical analysis of a large number of simulated trajectories. All trajectory calculations were performed using the chemical-reaction kinetics program VENUS96[34]. The initial spatial phase angles and internuclear distances for each trajectory are determined by random sampling via the Monte Carlo method, and the impact parameter b is sampled as $b = \xi^{1/2} b_{max}$, where ξ is a random number between 0 and 1, and b_{max} is the maximum impact parameter. Convergence tests with batches of trajectories showed that setting $b_{max} = 6$ Å is sufficient to cover all relevant reaction processes. Vibrational energy levels of product molecules are assigned using the Einstein–Brillouin–Keller (EBK) semiclassical approximation[35], with results rounded to the nearest integer. The probability of a reaction event i occurring in a STS collision with initial translational

energy E_t is calculated by the following equation:

$$P_i(E_t) \approx \frac{N_i}{N_{\text{total}}} \tag{9}$$

Where reaction event $i \in \{$ VTN, VTO, VVN, VVO, O_2 single dissociation, N_2 single dissociation, exchange dissociation, double dissociation $\}$; N_i refers to the number of trajectories in which the reaction event occurs i; N_{total} is the total number of trajectories in the simulation run. The scattering cross section σ for reaction event i is expressed as

$$\sigma_i\ (E_t) \approx \pi b_{\max}^2 \frac{N_i}{N_{\text{total}}} \tag{10}$$

The corresponding statistical error due to Monte Carlo sampling is

$$\Delta\sigma_i\ (E_t) = \sigma_i\ (E_t) \sqrt{\frac{N_{\text{total}} - N_i}{N_{\text{total}} N_i}} \tag{11}$$

and the reaction rate coefficient at translational temperature T is given by

$$k_i\ (T) = \frac{1}{k_B T}\left(\frac{8}{\pi\mu k_B T}\right)^{1/2} \int_0^\infty \sigma_i\ (E_t)\ \exp\left(-\frac{E_t}{k_B T}\right) E_t \mathrm{d}E_t \tag{12}$$

where k_B is the Boltzmann constant, μ is the reduced mass, and T (in K) is the translational temperature corresponding to the relative translational energy E_t. In all QCT calculations, the initial rotational states are set to the ground level, i.e., $N_2(v,j=0)+O_2(w,m=0)$. The initial and final distances between the molecular centroids are set to 15 Å. To ensure energy and angular-momentum conservation, the time step was chosen as 0.05 fs after a series of tests. The reaction cross sections are evaluated for initial translational energies from 0.2 to 10 eV, and the reaction rate coefficients correspond to translational temperatures from 5000 to 30000 K. Each simulation runs 10^5 trajectories, amounting to a cumulative total of about 10^8 trajectories.

The calculations employ the high-accuracy ab initio potential-energy surface (PES) for the electronic ground state of the N_2-O_2 system constructed by Truhlar *et al.*[18] The PES is based on multi-configuration complete-active-space second-order perturbation theory with an augmented correlation-consistent polarized triple-zeta basis set and external correlation corrections. Energy data points obtained from these calculations were fitted using permutation-invariant polynomials to represent the many-body interactions. Besides inelastic collisions, the PES can describe all possible dissociation and recombination channels in N_2-O_2 collisions and has been used repeatedly to study high-energy vibration–rotation energy transfer and collision-induced dissociation processes[19,36–38,14]. To validate the PES, we calculated the rate coefficients for the VT process $(1,0) \rightarrow (0,0)$ and the VV process $(1,0) \rightarrow (0,1)$ and compared them with earlier results[25,39], as shown in Fig. 1. Fig. 1 demonstrates that the present VV and VT transition results agree well with previous theoretical data at

temperatures above 3000 K, particularly with the semiclassical results of Garcia *et al.*[25] obtained on an empirical potential surface. These comparisons indicate that the adopted PES accurately describes both long-range and short-range interactions in the high-temperature regime, confirming its suitability for studying high-temperature collision energy transfer. They also verify the reliability of the present dynamical calculations.

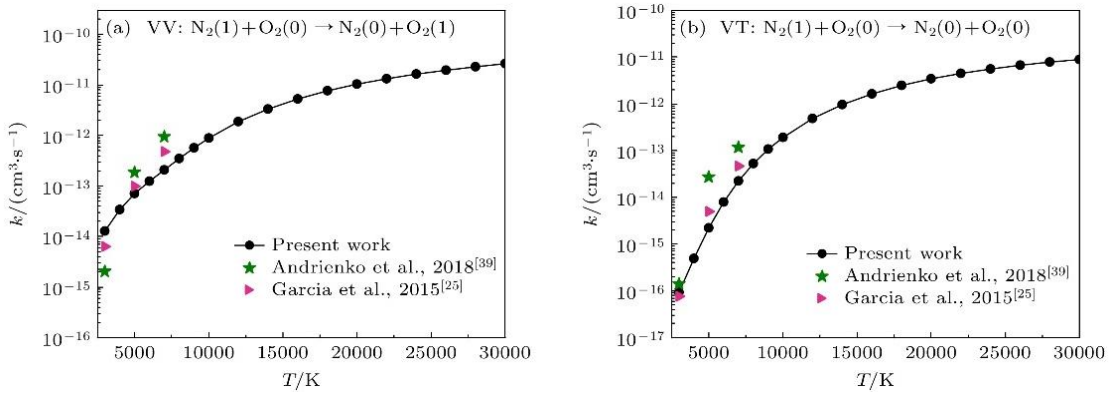

Figure 1. Rate coefficients for the (a) VV process (1,0) → (0,1) and (b) VT process (1,0) → (0,0) as functions of translational temperature. Present results (solid black lines) are compared with earlier theoretical data[25,39].

2.2 Neural network model

Neural networks are a widely used computational model in machine learning. Inspired by the structure of biological neural networks, they consist of interconnected nodes (neurons) organized into layers, enabling them to learn complex mappings from input to output. A back-propagation neural network (BP-NN)[40] is employed to predict the dissociation process in the N_2-O_2 collision system based on QCT-computed dissociation cross-section data. The network comprises an input layer, four hidden layers, and an output layer. Five input features are used to describe the STS collision-induced dissociation process: (1) the relative translational energy E_t; (2) the initial vibrational quantum numbers v and w; (3) the initial vibrational-rotational energies E_{int1} and E_{int2}. The output layer gives the total dissociation cross-section σ for the specified vibrational state. The four hidden layers contain 40, 10, 4, and 4 neurons, respectively. Before training, both input and output variables are normalized via

$$x_{\text{rescaled}} = a + \frac{b-a \quad x - x_{\min}}{x_{\max} - x_{\min}} \tag{13}$$

Here a and b are set to −1 and 1, x and x_{rescaled} denote the original and normalized variables, and $x_{\max}$ and $x_{\min}$ are the maximum and minimum values of each variable. The sigmoid function, $\text{sig}(x) = (1+e^{-x})^{-1}$, is chosen as the activation function. The mean squared error (MSE) is adopted as the loss function:

$$\tau = \frac{1}{n}\sum_{i=1}^{n} \left| Y_i - Y_i^{'} \right|^2 \tag{14}$$

where n is the number of samples, Y_i denotes the QCT-computed value, and $Y_i^{'}$ is the NN-predicted value. The Levenberg–Marquardt algorithm optimizes the weight and bias matrices[41]. To balance accuracy and efficiency, the training stops when the MSE falls below 10^{-6} or after a maximum of 10^3 iterations. The QCT dataset is split into a training set (80%) and a test set (20%). To ensure representative coverage, QCT calculations were carried out for two groups of initial vibrational quantum-number combinations, as listed in Tab. 1. Together, the two batches cover 90 distinct $N_2(v)+O_2(w)$ collision processes, corresponding to approximately 8.06% of all possible STS combinations within $v_{max} = 35$ and $w_{max} = 30$. The resulting dataset comprises 1104 data points, each containing the five input features (E_t,v,w,E_{int1},E_{int2}) and the corresponding dissociation cross-section σ.

Table 1. $N_2(v)+O_2(w)$ collision processes contained in the QCT dataset.

Group	$N_2(v)$	$O_2(w)$	E_t (eV)
1	{0, 5, 10, 21, 30}	{0, 1, 3, 7, 10, 15, 21, 25, 30}	{0.2, 0.6, 1, 2, 3, 4, 5, 6, 7, 8, 9, 10}
2	{0, 1, 3, 7, 10, 15, 21, 25, 30, 35}	{0, 5, 10, 21, 30}	

3. Results and Discussion

3.1 Inelastic VV/VT reaction cross sections and rate coefficients

The distributions of vibration-rotation energy levels and the dissociation energy thresholds differ between $N_2(v)$ and $O_2(w)$, leading to distinct theoretical behaviors of their vibrational transition processes. Therefore, for any $N_2(v)+O_2(w)$ collision with given initial vibrational-rotational states, the vibrational energy-transfer processes—VVN, VVO, VTN, and VTO, defined in (1)–(4)—are analyzed separately for the two molecules.

Fig. 2 presents contour plots of VVN and VVO single-quantum transition cross sections versus the initial vibrational level v and translational energy E_t for the processes $N_2(v)+O_2(10)$, $N_2(v)+O_2(21)$, and $N_2(v)+O_2(30)$. To facilitate direct comparison of the VVN and VVO magnitudes, contour maps for the same collision process are plotted on identical scales. Fig. 2 reveals that the dependences of VVN and VVO cross sections on translational energy and initial vibrational level are qualitatively similar across the three collision systems, with VVO cross sections being slightly larger. For $N_2(v)+O_2(10)$ collisions, both VVN and VVO cross sections at fixed E_t first rise with increasing v and then level off. At fixed v, the VVN and VVO cross sections show a non-monotonic dependence on translational energy, rising to a maximum before declining. For $N_2(v)+O_2(21)$ and $N_2(v)+O_2(30)$, the VV cross sections display a more complex dependence on v, particularly in the low-energy collision regime. For instance, in $N_2(v)+O_2(21)$ collisions at low energy ($E_t < 1$eV), both VVN and VVO exhibit two

maxima near $v \approx 5$ and $v \approx 20$, with minima around $v \approx 15$ and $v \approx 30$.

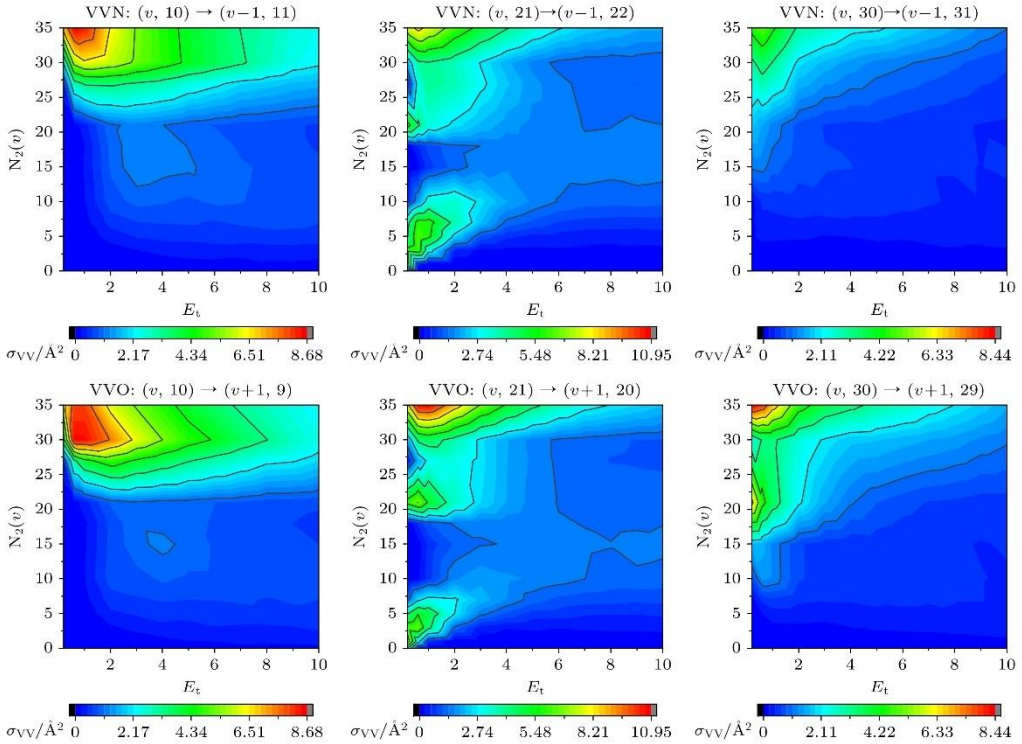

Figure 2. Contour map of VVN and VVO single-quantum transition cross sections as functions of the initial vibrational level v and translational energy E_t for the processes $N_2(v)+O_2(10)$, $N_2(v)+O_2(21)$, and $N_2(v)+O_2(30)$.

Fig. 3 shows contour plots of VTN and VTO single-quantum transition cross sections versus the initial vibrational level v and translational energy E_t for $N_2(v)+O_2(10)$, $N_2(v)+O_2(21)$, and $N_2(v)+O_2(30)$. To allow direct comparison, contour maps for the same collision process share a common color scale. In all three systems, the VTO cross sections are much larger than the VTN values. For $N_2(v)+O_2(21)$ and $N_2(v)+O_2(30)$, the VTN contributions are negligibly small. This arises because O_2 has smaller inter-vibrational level spacings than N_2, making its vibrational modes more readily excited. Compared with VVO transitions, VTO transitions exhibit a stronger dependence on translational energy: while VTO for $w = 10$ increases with E_t, it decreases for $w = 21$, and for $w = 30$ it first decreases and then rises. When low-lying excited O_2 ($w = 10, 21$) collides with low-v N_2 ($0 \le v \le 20$), the VVO cross section is markedly smaller than VTO. In collisions with high-energy N_2 ($20 < v \le 35$), however, the VVO cross section becomes notably larger than that of VTO. For highly excited $O_2(30)$ colliding with N_2 ($0 < v \le 30$), the VTO cross section exceeds the VVO cross section across the entire studied energy range ($0 < E_t \le 10$ eV). This behavior stems from the distinct dissociation thresholds and energy-level distributions of the two molecules. Moreover, VV transitions between different excited states can be suppressed by competing channels—such as exchange, dissociation, or asymmetric multi-quantum resonance processes that involve smaller energy mismatches.

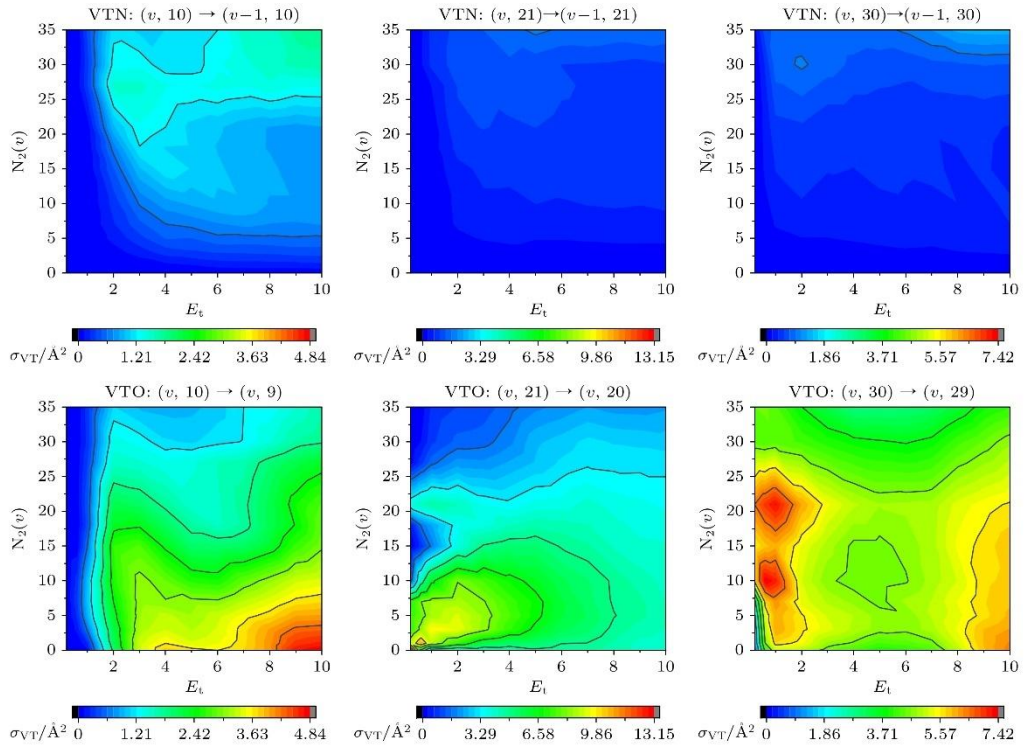

Figure 3. Contour map of VTN and VTO single-quantum transition cross sections as functions of the initial vibrational level v and translational energy E_t for the processes $N_2(v)+O_2(10)$, $N_2(v)+O_2(21)$, and $N_2(v)+O_2(30)$.

The contour maps of VV and VT cross sections reveal distinct contributions of single- quantum VV and VT transitions when O_2 collides with N_2 molecules in different vibrational states v. Fig. 4 shows the temperature dependence (5000–30000 K) of single- and multi- quantum VVO and VTO reaction rate coefficients for six sets of N_2+O_2 collisions. For vibrationally excited $O_2(w = 10, 30)$, three types of collision partners are examined: (a)–(b), vibrationally ground- state $N_2(v = 0)$; (c)–(d), moderately excited $N_2(v = 15)$; and (e)–(f), highly excited $N_2(v = 35)$. As temperature rises, both VVO and VTO rate coefficients grow for $O_2(w)$–$N_2(v = 0)$ and $O_2(w)$–$N_2(v = 15)$ collisions. For $O_2(w)$–$N_2(v = 35)$, the VTO coefficient also increases with temperature, whereas the VVO coefficient remains nearly constant. This occurs because the dissociation channel preferentially consumes highly excited molecules, thereby suppressing high- energy VV transitions[36,42]. When O_2 collides with ground- state $N_2(v = 0)$, the rate coefficients for both single- and multi- quantum VTO channels significantly exceed those for VVO. As the N_2 vibrational level rises, the VTO coefficients decrease while the VVO coefficients increase. For example, in Fig. 4(f), which corresponds to collisions between two highly excited molecules, the single- and multi- quantum VVO and VTO coefficients become comparable, especially above 20000 K. In general, for a fixed $N_2(v)$ molecule, vibrational energy transfer becomes more efficient as the partner $O_2(w)$ level increases; conversely, for a fixed $O_2(w)$, transfer efficiency tends to decrease with increasing $N_2(v)$. Unlike the previously studied N_2-N_2 system[31], the VV and VT trends in N_2-O_2 collisions exhibit greater complexity due to the dissimilar energy- level structures of the two molecules. Their evolution with vibrational- rotational

energy cannot be described simply in terms of the initial vibrational- energy spacing.

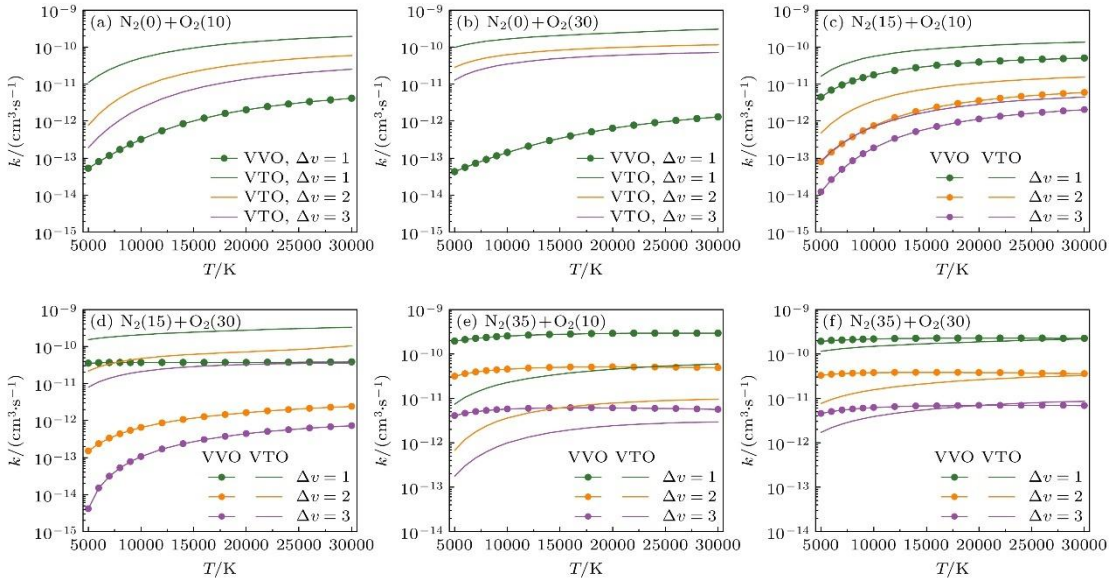

Figure 4. Temperature dependence of single- and multi-quantum VVO and VTO rate coefficients for different $N_2(v)$-$O_2(w)$ collisions.

To facilitate implementation in kinetic modeling, the VV and VT rate coefficients can be fitted to the Arrhenius form:

$$k\ T\ = AT^{n}\exp\ -B/T \tag{15}$$

Here, A, n, and B are fitting parameters, and T is the translational temperature in the range 5000–30000 K. Fitted parameters for selected processes are listed in Table A1 of the Appendix. The MSE of the fits is on the order of 10^{-27}.

3.2 Reaction cross section of each dissociation channel

The dissociation channels in N_2-O_2 collisions comprise O_2 single- dissociation, N_2 single- dissociation, exchange- dissociation (yielding one NO molecule), and double- dissociation, as defined in (5)–(8). The total dissociation cross section is obtained from

$$\sigma_{total-dissoc} = \sigma_{N_2-dissoc} + \sigma_{O_2-dissoc} + \sigma_{exchange-dissoc} + 2\sigma_{double-dissoc} \tag{16}$$

Fig. 5 and Fig. 6 present contour maps of the reaction cross sections for each dissociation channel as functions of the initial translational energy E_t and the initial vibrational levels v (N_2) or w (O_2), respectively. The double- dissociation channel is omitted from the individual panels due to its small cross section; its contribution is nonetheless included in the total dissociation cross section. To permit direct comparison of the contributions from different channels, contour maps for the same collision process share a common color scale. Because the dissociation energy of O_2 (5.21 eV) is lower than that of N_2 (9.90 eV), the O_2 single- dissociation cross section is substantially larger than the N_2

single- dissociation cross section in all cases. As seen in Fig. 5, the O_2 single- dissociation cross section varies only weakly with the N_2 vibrational level v. In contrast, Fig. 6 shows that it grows markedly with the O_2 vibrational level w. Thus, the O_2 single- dissociation cross section is primarily governed by the initial O_2 vibrational level and is much less sensitive to the vibrational state of the N_2 partner. Moreover, the translational energy thresholds for single- and exchange- dissociation decrease with rising initial vibrational energy. The corresponding cross sections increase with translational energy before eventually saturating. As both vibrational levels and the translational energy rise, the total energy may surpass the thresholds for exchange- and double- dissociation. Under such conditions, single- dissociation events become partially suppressed, and their cross sections can fall below those of the exchange- dissociation channel. Overall, regardless of the relative contributions of individual channels, the total dissociation cross section increases with vibrational level and translational energy until saturation is reached.

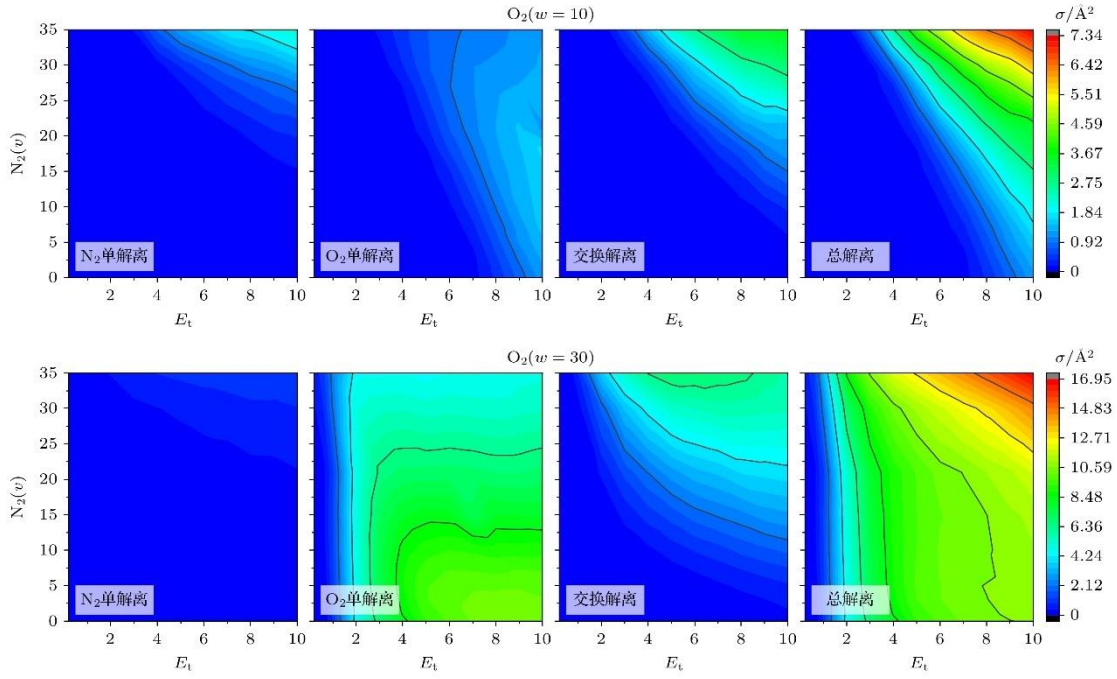

Figure 5. Contour maps of dissociation reaction cross sections versus the initial N_2 vibrational level v and translational energy E_t.

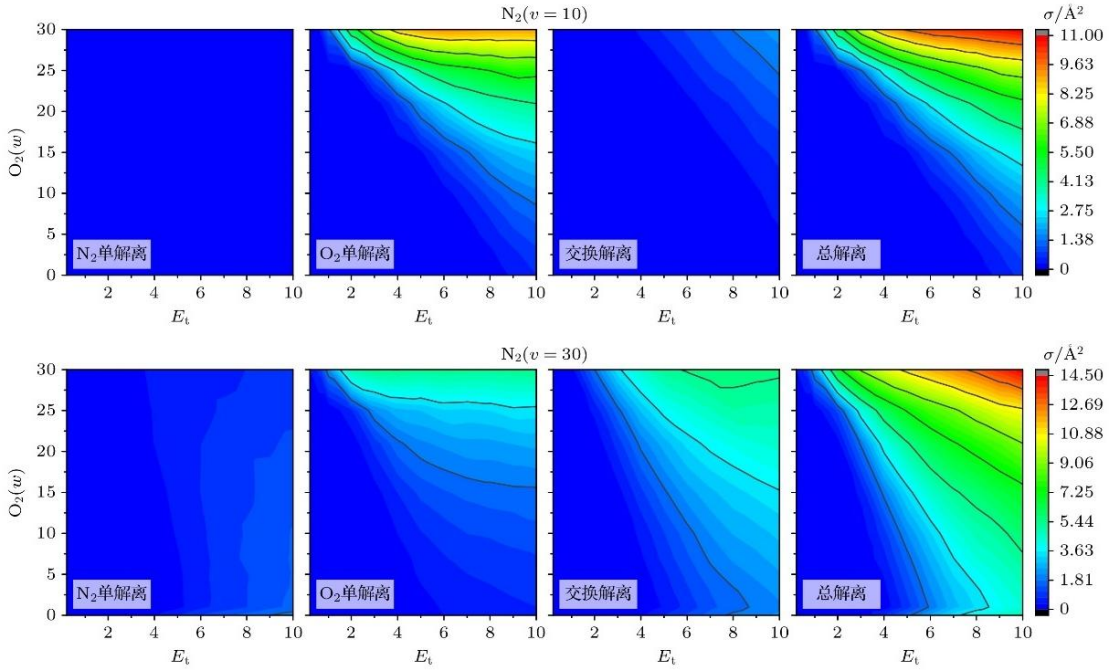

Figure 6. Contour maps of dissociation reaction cross sections versus the initial O_2 vibrational level w and translational energy E_t.

3.3 The NN-totaldiss model

Single- and exchange-dissociation channels can be either promoted or suppressed as translational and initial vibrational energies vary, whereas the total dissociation cross section increases monotonically. Leveraging this monotonic trend and the QCT-computed dataset of total dissociation cross sections, we constructed a neural-network model, termed NN-totaldiss, that directly predicts the total dissociation cross sections for collisions between designated vibrational states of N_2 and O_2. Because dissociation requires the total energy to exceed the dissociation threshold, the following dynamical parameters are chosen as input features: the initial translational energy E_t, the initial vibrational-rotational energies of the two molecules ((E_{int1}, E_{int2}), and the initial vibrational quantum numbers (v, w).

As shown in the Fig. 7, the R-value for both the training and test sets of the NN-totaldiss model reaches 0.99. The MSE are about 0.0145 and 0.0582, respectively, and most predicted cross sections differ from the QCT values by less than 0.2 $Å^2$, confirming the reliability and accuracy of the model. Contour maps of the total dissociation cross section predicted by the NN-totaldiss model versus the initial translational energy E_t and the initial quantum numbers w (O_2) and v (N_2) are provided in Fig. 8. Fig. 8 demonstrates that the NN-totaldiss predictions agree well with the QCT results both in magnitude and in their variation with translational energy and the two initial quantum numbers. Thus, the model faithfully captures the evolution of the total dissociation cross section with translational energy and the initial quantum numbers of N_2 and O_2. Owing to the finite number of simulated trajectories and Monte-Carlo sampling errors, some numerical uncertainty remains when predicting

vanishingly small cross sections. Overall, the NN- totaldiss model provides an efficient and accurate tool for predicting total dissociation cross sections in STS N_2-O_2 collisions.

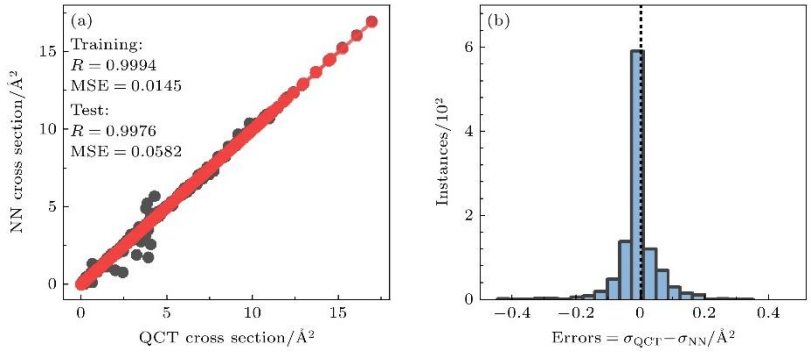

Figure 7. (a) Comparison between the NN- predicted and the raw QCT- computed total dissociation cross sections. (b) Histogram of the prediction errors. The black dashed line marks zero error.

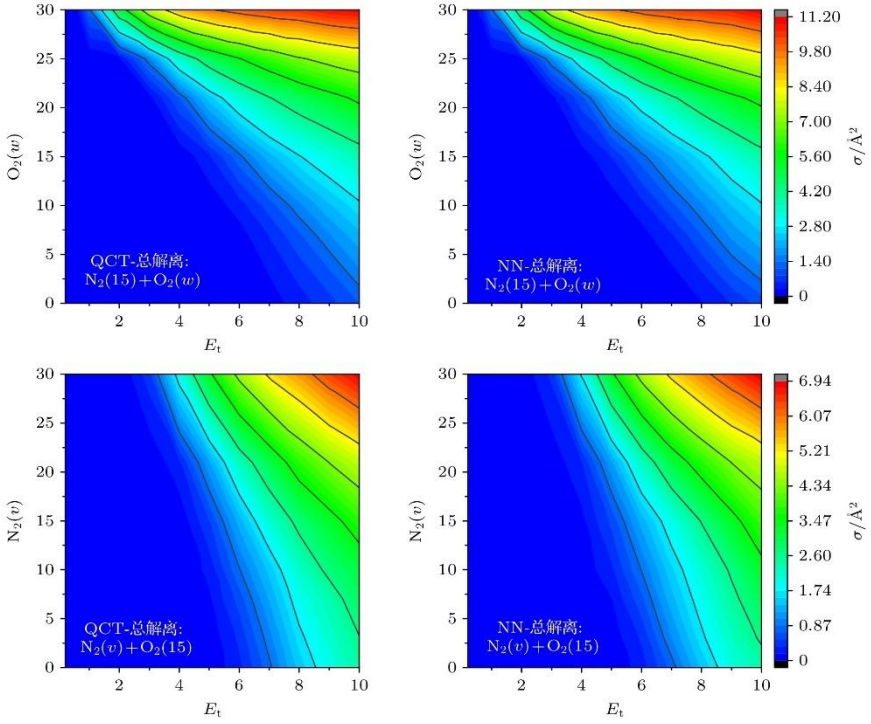

Figure 8. Contour maps of the total dissociation cross section versus the initial vibrational levels of $O_2(w)$ and $N_2(v)$ and translational energy E_t: QCT- calculated (left) and NN- predicted (right) results.

For convenient use in kinetic simulations, the total dissociation cross sections are represented by the analytical form[43]

$$\sigma_{total-dissoc} = 10^{a/E_t^2 + b/E_t + c} \tag{17}$$

with fitted parameters *a*, *b*, and *c*. The expression applies over the translational energy range 0.2–10 eV. Parameters for selected processes are given in Table A2 (Appendix); the root- mean- square error (RMSE) of the fits is typically on the order of 10^{-4}.

4. Conclusion

The STS collisional energy‑transfer processes in N_2-O_2 have been investigated in detail using QCT calculations and a NN model. First, QCT calculations were performed for 90 distinct initial vibrational‑state combinations of $N_2(v)$+$O_2(w)$. The contributions of inelastic VV/VT transitions, single‑dissociation of N_2 and O_2, exchange‑dissociation, and double‑dissociation channels, together with the dependence of their cross sections on energy, were systematically analyzed. Furthermore, the temperature dependence (5000–30000 K) of single‑ and multi‑quantum VV/VT rate coefficients was examined. The main findings are:

(1) For near‑resonance VV transitions, the de‑excitation probabilities of N_2 and O_2 are comparable, whereas the VT transition probability of O_2 is markedly higher than that of N_2;

(2) The O_2 single‑dissociation channel dominates, followed by the N_2-O_2 exchange‑dissociation channel, while N_2 single‑ and double‑dissociation channels contribute much less;

(3) The total dissociation cross section increases monotonically with increasing vibrational and translational energy.

Using the QCT‑computed dataset of total dissociation cross sections, a high‑performance NN‑totaldiss model ($R \approx 0.99$) was trained to accurately predict the total dissociation cross section for specified $N_2(v)$+$O_2(w)$ collisions. Compared with pure QCT calculations, the hybrid QCT‑NN approach reduces the computational cost by approximately 91.94 %. This work offers a useful framework for studying energy transfer in other molecule-molecule systems and provides practical data for refining non‑thermal‑equilibrium kinetic models.

Acknowledgements

Project supported by the National Key R&D Program of China (Grant No. 2024YFF0508503).

Appendix: Fitting Parameters for VV/VT reaction rate coefficients and total dissociation cross sections

Table A1. Arrhenius parameters (A, n, B) for the VV/VT reaction rate coefficient $k(T)$ (in $cm^3 \cdot s^{-1}$). The fits cover the temperature range 5000–30000 K; MSE denotes the mean squared error (in $cm^3 \cdot s^{-1}$).

$N_2(v)$+$O_2(w)$→$N_2(v')$+$O_2(w')$	A	n	B	MSE
(0, 10) → (1, 9)	4.10×10^{-10}	-2.91×10^{-1}	4.81×10^{4}	4.27×10^{-26}
(0, 10) → (0, 9)	2.44×10^{-10}	4.28×10^{-2}	2.01×10^{4}	7.67×10^{-22}
(0, 10) → (0, 8)	3.33×10^{-10}	-6.70×10^{-2}	3.10×10^{4}	3.04×10^{-23}
(0, 10) → (0, 7)	3.95×10^{-10}	-1.39×10^{-1}	3.96×10^{4}	2.66×10^{-24}
(0, 21) → (1, 20)	4.24×10^{-10}	-4.58×10^{-1}	-4.53×10^{3}	4.21×10^{-23}
(0, 21) → (0, 20)	3.50×10^{-10}	2.04×10^{-1}	2.78×10^{3}	7.96×10^{-21}
(0, 21) → (0, 19)	2.51×10^{-10}	-3.01×10^{-2}	1.94×10^{4}	2.32×10^{-22}
(0, 21) → (0, 18)	2.87×10^{-10}	-7.43×10^{-2}	2.46×10^{4}	5.62×10^{-23}
(0, 30) → (1, 29)	3.01×10^{-10}	-3.75×10^{-1}	4.79×10^{4}	6.99×10^{-27}

(0, 30) → (0, 29)	1.39×10^{-10}	9.46×10^{-2}	7.06×10^{3}	6.44×10^{-21}
(0, 30) → (0, 28)	1.49×10^{-10}	2.78×10^{-3}	9.00×10^{3}	9.18×10^{-22}
(0, 30) → (0, 27)	1.74×10^{-10}	-5.01×10^{-2}	1.14×10^{4}	2.99×10^{-22}
(15, 10) → (16, 9)	2.31×10^{-10}	-9.11×10^{-2}	1.73×10^{4}	8.85×10^{-23}
(15, 10) → (17, 8)	3.46×10^{-10}	-2.77×10^{-1}	3.64×10^{4}	2.77×10^{-25}
(15, 10) → (18, 7)	3.94×10^{-10}	-3.69×10^{-1}	4.36×10^{4}	1.97×10^{-26}
(15, 10) → (15, 9)	1.97×10^{-10}	5.51×10^{-3}	1.30×10^{4}	8.14×10^{-22}
(15, 10) → (15, 8)	2.78×10^{-10}	-1.96×10^{-1}	2.58×10^{4}	4.40×10^{-24}
(15, 10) → (15, 7)	3.17×10^{-10}	-3.04×10^{-1}	3.38×10^{4}	2.16×10^{-25}
(15, 21) → (16, 20)	1.79×10^{-10}	-2.61×10^{-2}	1.56×10^{4}	2.42×10^{-22}
(15, 21) → (17, 19)	2.69×10^{-10}	-3.02×10^{-1}	2.64×10^{4}	5.21×10^{-25}
(15, 21) → (18, 18)	3.12×10^{-10}	-3.82×10^{-1}	3.60×10^{4}	3.42×10^{-26}
(15, 21) → (15, 20)	1.96×10^{-10}	7.64×10^{-2}	1.35×10^{4}	2.82×10^{-21}
(15, 21) → (15, 19)	2.46×10^{-10}	-1.03×10^{-1}	2.19×10^{4}	3.80×10^{-23}
(15, 21) → (15, 18)	2.07×10^{-10}	-1.88×10^{-1}	2.49×10^{4}	3.33×10^{-24}
(15, 30) → (16, 29)	9.24×10^{-11}	-8.39×10^{-2}	1.39×10^{3}	3.39×10^{-22}
(15, 30) → (17, 28)	2.05×10^{-10}	-3.47×10^{-1}	2.70×10^{4}	1.23×10^{-25}
(15, 30) → (18, 27)	3.20×10^{-10}	-4.66×10^{-1}	3.90×10^{4}	4.67×10^{-27}
(15, 30) → (15, 29)	1.17×10^{-10}	1.13×10^{-1}	4.53×10^{3}	1.04×10^{-20}
(15, 30) → (15, 28)	1.57×10^{-10}	-1.67×10^{-2}	1.10×10^{4}	5.05×10^{-22}
(15, 30) → (15, 27)	5.12×10^{-10}	-2.19×10^{-1}	1.17×10^{4}	1.06×10^{-22}
(35, 10) → (36, 9)	5.68×10^{-10}	-5.32×10^{-2}	3.17×10^{3}	1.51×10^{-20}
(35, 10) → (37, 8)	1.30×10^{-9}	-2.97×10^{-1}	6.01×10^{3}	4.83×10^{-22}
(35, 10) → (38, 7)	4.10×10^{-10}	-3.94×10^{-1}	6.35×10^{3}	7.64×10^{-24}
(35, 10) → (35, 9)	2.01×10^{-10}	-6.83×10^{-2}	1.58×10^{4}	1.33×10^{-22}
(35, 10) → (35, 8)	1.98×10^{-10}	-2.33×10^{-1}	1.85×10^{4}	3.73×10^{-24}
(35, 10) → (35, 7)	1.88×10^{-10}	-3.31×10^{-1}	2.17×10^{4}	3.19×10^{-25}
(35, 21) → (36, 20)	1.79×10^{-10}	-2.60×10^{-2}	1.56×10^{4}	2.42×10^{-22}
(35, 21) → (37, 19)	2.69×10^{-10}	-3.02×10^{-1}	2.64×10^{4}	5.21×10^{-25}
(35, 21) → (38, 18)	3.12×10^{-10}	-3.82×10^{-1}	3.60×10^{4}	3.4×10^{-26}
(35, 21) → (35, 20)	1.96×10^{-10}	7.64×10^{-2}	1.35×10^{4}	2.82×10^{-21}
(35, 21) → (35, 19)	2.46×10^{-10}	-1.03×10^{-1}	2.19×10^{4}	3.80×10^{-23}
(35, 21) → (35, 18)	2.07×10^{-10}	-1.88×10^{-1}	2.49×10^{4}	3.33×10^{-24}
(35, 30) → (36, 29)	5.99×10^{-10}	-8.87×10^{-2}	1.96×10^{3}	1.15×10^{-20}
(35, 30) → (37, 28)	4.54×10^{-10}	-2.35×10^{-1}	3.14×10^{3}	3.48×10^{-22}
(35, 30) → (38, 27)	9.69×10^{-11}	-2.38×10^{-1}	5.53×10^{3}	9.00×10^{-24}
(35, 30) → (35, 29)	6.49×10^{-11}	1.25×10^{-1}	3.21×10^{3}	5.24×10^{-21}
(35, 30) → (35, 28)	1.25×10^{-10}	-9.18×10^{-2}	1.26×10^{4}	6.00×10^{-23}
(35, 30) → (35, 27)	1.61×10^{-10}	-2.35×10^{-1}	1.59×10^{4}	3.84×10^{-24}

Table A2. Parameters (a, b, c) for the total dissociation cross-section fit $\sigma_{tot}(E_t)$ (in Å^2). The fit is valid for initial translational energies $E_t = 0.2$–10 eV; RMSE is the root-mean-square error (in Å^2).

$N_2(v)$	$O_2(w)$	a	b	c	RMSE
0	1	1.98×10^{1}	-1.02×10^{2}	9.03×10^{0}	1.82×10^{-4}
0	3	1.13×10^{1}	-5.82×10^{1}	5.11×10^{0}	3.54×10^{-4}
0	5	8.29×10^{0}	-4.30×10^{1}	3.87×10^{0}	2.95×10^{-3}
0	7	6.43×10^{0}	-3.35×10^{1}	3.14×10^{0}	8.48×10^{-3}

0	10	-2.46×10^{2}	3.52×10^{1}	-9.70×10^{-1}	5.70×10^{-3}
0	15	-9.18×10^{1}	1.06×10^{1}	2.57×10^{-1}	8.02×10^{-3}
0	21	-2.04×10^{1}	2.24×10^{-1}	8.60×10^{-1}	3.37×10^{-2}
0	25	-5.67×10^{0}	-1.11×10^{0}	1.01×10^{0}	6.37×10^{-2}
0	30	-6.06×10^{-1}	-5.62×10^{-1}	1.10×10^{0}	1.30×10^{-1}
1	21	-2.03×10^{1}	3.57×10^{-1}	8.50×10^{-1}	2.33×10^{-2}
1	30	-7.54×10^{-1}	-4.60×10^{-1}	1.09×10^{0}	1.58×10^{-1}
3	15	-7.75×10^{1}	8.74×10^{0}	3.16×10^{-1}	1.44×10^{-2}
3	21	-2.10×10^{1}	1.02×10^{0}	7.94×10^{-1}	4.72×10^{-2}
3	30	-8.40×10^{-1}	-3.81×10^{-1}	1.09×10^{0}	1.73×10^{-1}
5	30	-8.07×10^{-1}	-3.74×10^{-1}	1.09×10^{0}	1.94×10^{-1}
5	0	8.27×10^{0}	-4.28×10^{1}	3.65×10^{0}	6.98×10^{-3}
5	1	8.21×10^{0}	-4.25×10^{1}	3.75×10^{0}	3.78×10^{-3}
5	3	7.21×10^{0}	-3.75×10^{1}	3.44×10^{0}	6.53×10^{-3}
5	7	-3.96×10^{2}	6.61×10^{1}	-2.62×10^{0}	1.60×10^{-3}
5	10	-2.83×10^{2}	4.83×10^{1}	-1.81×10^{0}	5.40×10^{-3}
5	15	-7.95×10^{1}	9.94×10^{0}	2.43×10^{-1}	2.80×10^{-2}
5	21	-1.95×10^{1}	8.26×10^{-1}	8.08×10^{-1}	3.42×10^{-2}
5	25	-6.46×10^{0}	-4.60×10^{-1}	9.66×10^{-1}	6.22×10^{-2}
7	15	-6.79×10^{1}	8.41×10^{0}	2.93×10^{-1}	2.57×10^{-2}
7	21	-1.85×10^{1}	6.82×10^{-1}	8.22×10^{-1}	3.75×10^{-2}
7	30	-7.52×10^{1}	-3.87×10^{-1}	1.09×10^{0}	2.02×10^{-1}
10	15	-6.21×10^{1}	7.99×10^{0}	3.14×10^{-1}	3.16×10^{-2}
10	21	-1.75×10^{1}	7.87×10^{-1}	8.16×10^{-1}	4.21×10^{-2}
10	30	-6.64×10^{-1}	-4.20×10^{-1}	1.09×10^{0}	2.00×10^{-1}
15	0	3.92×10^{0}	-2.04×10^{1}	2.03×10^{0}	1.68×10^{-2}
15	3	3.21×10^{0}	-1.68×10^{1}	1.83×10^{0}	4.68×10^{-2}
15	7	-1.97×10^{2}	3.56×10^{1}	-1.29×10^{0}	2.32×10^{-2}
15	10	-1.12×10^{2}	1.78×10^{1}	-2.20×10^{-1}	3.96×10^{-2}
15	15	-4.74×10^{1}	5.30×10^{0}	5.20×10^{-1}	3.20×10^{-2}
15	21	-1.20×10^{1}	-4.00×10^{-1}	9.19×10^{-1}	5.88×10^{-2}
15	25	-5.0×10^{0}	-5.65×10^{-1}	9.88×10^{-1}	3.51×10^{-2}
15	30	-6.92×10^{-1}	-3.97×10^{-1}	1.09×10^{0}	1.50×10^{-1}
18	21	-1.16×10^{1}	-2.55×10^{-1}	9.34×10^{-1}	5.33×10^{-2}
21	15	-3.44×10^{1}	4.04×10^{0}	6.22×10^{-1}	4.97×10^{-2}
21	0	-7.70×10^{1}	5.01×10^{0}	5.89×10^{-1}	1.06×10^{-2}
21	1	-7.61×10^{1}	5.57×10^{0}	5.54×10^{-1}	7.48×10^{-3}
21	3	-8.50×10^{1}	9.82×10^{0}	2.65×10^{-1}	1.68×10^{-2}
21	7	-6.54×10^{1}	7.75×10^{0}	3.69×10^{-1}	2.71×10^{-2}
21	10	-4.66×10^{1}	4.61×10^{0}	5.73×10^{-1}	1.65×10^{-2}
21	18	-1.81×10^{1}	8.87×10^{-1}	8.42×10^{-1}	6.70×10^{-2}
21	21	-1.09×10^{1}	8.07×10^{-2}	9.19×10^{-1}	5.56×10^{-2}
21	25	-3.91×10^{0}	-8.38×10^{-1}	1.04×10^{0}	6.94×10^{-2}
21	27	-2.07×10^{0}	-7.80×10^{-1}	1.07×10^{0}	6.97×10^{-2}
21	30	-4.61×10^{-1}	-5.58×10^{-1}	1.12×10^{0}	1.79×10^{-1}
27	21	-6.79×10^{0}	-4.70×10^{-1}	1.02×10^{0}	8.37×10^{-2}
30	15	-9.22×10^{0}	-3.68×10^{-1}	9.65×10^{-1}	1.25×10^{-1}
30	21	-4.34×10^{0}	-9.02×10^{-1}	1.08×10^{0}	1.40×10^{-1}
30	30	1.01×10^{-1}	-8.90×10^{-1}	1.23×10^{0}	3.85×10^{-1}

35	21	-2.49×10^{0}	-8.65×10^{-1}	1.13×10^{0}	1.79×10^{-1}
35	5	-1.15×10^{1}	5.75×10^{-1}	8.62×10^{-1}	5.73×10^{-2}
35	10	-8.09×10^{0}	-4.55×10^{-2}	9.44×10^{-1}	7.15×10^{-2}
35	30	1.06×10^{-1}	-8.47×10^{-1}	1.29×10^{0}	5.14×10^{-1}

References

[1] Wang Q Y, Cong K L, Liu L L, Lu H Z, Xu S J 2017 Phys. Gases **2** 46

[2] Lu D R, Chen Z Y, Guo X, Tian W S 2009 Adv. Mech. **39** 674

[3] Dong W Z, DIing M S, Gao T S, Jiang T 2013 Acta Aerodyn. Sin. **31** 692

[4] Guo Y J, Zeng L, Zhang H Y, Dai G Y, Wang A L, Qiu B, Zhou S G, Liu X 2017 Acta Aerodyn. Sin. **35** 496

[5] Cacciatore M 1996 Mol. Phys. Hypersonic Flows **482** 21

[6] Pavlov A V 2011 Geomag. Aeron. 51 143

[7] Treanor C E 1965 J. Chem. Phys. **43** 532

[8] Nagnibeda E, Papina K, Kunova O 2018 AIP Conf. Proc. **1** 060012

[9] Laux C O, Pierrot L, Gessman R J 2012 Chem. Phys. **398** 46

[10] Zhao X, Xu X, Xu H 2024 J. Chem. Phys. **161** 231101

[11] Hong Q, Bartolomei M, Pirani F, Sun Q, Coletti C 2025 J. Chem. Phys. **162** 114308

[12] Feng D, Song Y, Wang Z, Yang L, Zhang Z, Yang Y 2025 J. Chem. Phys. **162** 114107

[13] He D, Liu T, Li R, Hong Q, Li F, Sun Q, Si T, Luo X 2024 J. Chem. Phys. **161** 244302

[14] Andrienko D, Boyd I D 2017 55th AIAA Aerospace Sciences Meeting Grapevine Texas, January 9-13, 2017 p2017-0659

[15] Kurnosov A K, Napartovich A P, Shnyrev S L, Cacciatore M 2010 Plasma Sources Sci. Technol. **19** 045015

[16] Esposito F, Garcia E, Lagan àA 2017 Plasma Sources Sci. Technol. **26** 045005

[17] Lino Da Silva M, Loureiro J, Guerra V 2012 Chem. Phys. Lett. **531** 28

[18] Varga Z, Meana-Pa ñeda R, Song G, Paukku Y, Truhlar D G 2016 J. Chem. Phys. **144** 024310

[19] Garcia E, Verdasco J E, Lagan àA 2020 J. Phys. Chem. A **124** 6445

[20] Andrienko D A, Boyd I D 2018 J. Chem. Phys. **148** 084309

[21] Garcia E, Pirani F, Lagan àA, Mart íC 2017 Phys. Chem. Chem. Phys. **19** 11206

[22] Garcia E, Lagan à A, Pirani F, Bartolomei M, Cacciatore M, Kurnosov A 2016 J. Phys. Chem. A **120** 5208

[23] Billing G D, Jolicard G 1982 Chem. Phys. **65** 323

[24] Billing G D 1994 Chem. Phys. **179** 463

[25] Garcia E, Kurnosov A, Lagan à A, Pirani F, Bartolomei M, Cacciatore M 2016 J. Phys. Chem. B **120** 1476

[26] Koner D, Unke O T, Boe K, Bemish R J, Meuwly M 2019 J. Chem. Phys. **150** 211101

[27] Chen J, Li J, Bowman J M, Guo H 2020 J. Chem. Phys. **153** 054310

[28] Hong Q, Storchi L, Bartolomei M, Pirani F, Sun Q, Coletti C 2023 Eur. Phys. J. D **77** 128
[29] Gu K M, Zhang H, Cheng X L 2023 J. Chem. Phys. **158** 244302
[30] Huang X, Gu K M, Guo C M, Cheng X L 2023 Phys. Chem. Chem. Phys. **25** 29475
[31] Guo C M, Zhang H, Cheng X L 2024 J. Phys. Chem. A **128** 5435
[32] Bernstein R B, Bederson B 1980 Phys. Today **33** 79
[33] Fernández-Ramos A, Miller J A, Klippenstein S J, Truhlar D G 2006 Chem. Rev. **106** 4518
[34] Hu X, Hase W L, Pirraglia T 1991 J. Comput. Chem. **12** 1014
[35] Gutzwiller M C 1990 Chaos in Classical and Quantum Mechanics (Berlin: Springer)
[36] Chaudhry R S, Bender J D, Valentini P, Schwartzentruber T E, Candler G V 2016 46th AIAA Thermophysics Conference Washington, June 13–17, 2016 p4319
[37] Mankodi T K, Bhandarkar U V, Myong R S 2020 Phys. Fluids **32** 036102
[38]Andrienko D, Boyd I D 2017 47th AIAA Thermophysics Conference Denver, Colorado, June 5–9, 2017 p3163
[39] Andrienko D, Boyd I D 2018 J. Thermophys. Heat Transfer **32** 904
[40] Rumelhart D E, Hintont G E, Williams R J 1986 Nature **323** 533
[41] Moré J J 1978 Numerical Analysis (Berlin, Heidelberg: Springer-Verlag) p105
[42] Chaudhry R S, Candler G V 2019 AIAA Scitech Forum San Diego, California, January 7–11, 2019 p2019-0789
[43] Mankodi T K, Bhandarkar U V, Puranik B P 2018 J. Chem. Phys. **148** 144305